

# ViscoReg: Neural Signed Distance Functions via Viscosity Solutions

Meenakshi Krishnan  
 Perceptual Interfaces and Reality Lab (PIRL)  
 Dept. of Mathematics  
 University of Maryland, College Park  
 mkrishn9@umd.edu

Ramani Duraiswami  
 Perceptual Interfaces and Reality Lab (PIRL)  
 UMIACS & Dept. of Computer Science  
 University of Maryland, College Park  
 ramanid@umd.edu

## Abstract

*Implicit Neural Representations (INRs) that learn a Signed Distance Function (SDF) are a powerful tool for continuous 3D scene reconstruction. These models are trained by enforcing the Eikonal equation. We demonstrate theoretically that despite the ill-posedness of the Eikonal equation, generalization error estimates may be obtained for Neural SDFs in terms of the training error. However, training with the Eikonal loss can lead to unstable gradient flows, necessitating alternate stabilization techniques. Traditional numerical solvers for the equation have relied on viscosity approaches for regularization. We enhance Neural SDF training using this well-developed theory, and introduce a new loss formulation we call ViscoReg. We theoretically demonstrate the stability of the gradient flow equation of our proposed loss term. Empirically, ViscoReg outperforms state-of-the-art approaches such as SIREN, DiGS, and StEik without adding significant computational cost.*

## 1. Introduction

Implicit neural representations (INR) have been used to encode continuous signals, such as images, sounds, 3D surfaces, or scenes [33, 35, 40]. Neural networks mapping input coordinates to signal values give compact, high-resolution, representations of the underlying signal. Neural Signed Distance Functions (SDFs) [40] extend this approach to 3D scene reconstruction by learning a function that maps spatial coordinates to their signed distance from the surface manifold comprising the scene. The surface is implicitly represented as the zero level set of the SDF. The input to the neural network model consists of point cloud data or images representing the projection of the scene. Training is supervised by constraining the signed distance to be zero on the surface and possibly using auxiliary information on surface normals. In the absence of normal information, earlier methods suffer from a severe degradation in reconstruction quality. While normals may be computed by

processing the input data using specialized algorithms, this is expensive and typically yields noisy estimates.

Several regularizations have been proposed to improve reconstruction quality. In the absence of the normal term, constraining the SDF to be zero on the surface manifold, could cause the network to degenerate to the trivial zero function. The widely used *Eikonal loss* ensures that the neural network learns a valid SDF by enforcing that it satisfies the Eikonal partial differential equation (PDE) [20]:

$$\|\nabla u(x)\|_2 = 1 \text{ for } x \in \Omega, \quad u(x) = 0 \text{ for } x \in \partial\Omega \quad (1)$$

Here,  $\Omega$  is an open connected bounded domain, and  $\partial\Omega$ , the sufficiently regular boundary surface we aim to reconstruct. However, simply enforcing the Eikonal loss without normal information does not lead to good reconstruction [5]. Moreover, instabilities arising during training when using the Eikonal loss can lead the network to converge to unsatisfactory local minima with large errors as recent studies have demonstrated, both theoretically and empirically [52]. These instabilities can be understood through analysis of the gradient flow differential equation arising in the continuum limit of the gradient descent formulation. Other regularizations that have been proposed either lack physical rigor (such as constraining the Eikonal to be harmonic [5]), require normals [4], or overfits noise in the input [52].

The Eikonal equation is inherently ill-posed, admitting multiple solutions (see Section 3 for details). The generalized Eikonal equation belongs to the broader class of Hamilton-Jacobi equations [16], for which the physically meaningful solutions in many applications are given by *viscosity solutions*. In particular, the SDF is the *unique* viscosity solution of the Eikonal equation, and can be recovered in the limit  $\varepsilon \rightarrow 0$  of solutions  $u_\varepsilon$  to the *well-posed* parabolic equation:

$$\|\nabla u_\varepsilon\|_2 = 1 + \varepsilon \Delta u_\varepsilon. \quad (2)$$

which adds a viscosity term to the Eikonal. This vanishing viscosity method is an important tool in the analysis

of these equations, and care is taken in classical numerical analysis to arrive at the viscosity solution rather than one of the infinitely many other Lipschitz solutions possible. For instance, the most popular Eikonal solver, Sethian’s Fast Marching method [44], is designed to compute viscosity solutions via level-set techniques, advancing the solution front in a causality-preserving manner. Motivated by these methods, we propose a novel regularization technique that incorporates a dynamically scaled viscous term into the training process of neural SDFs.

We also seek to address the important question, in context of INR-based SDF reconstruction: *given the infinitely many solutions to the Eikonal equation, why would minimizing the PDE residual and boundary loss at a finite set of points necessarily let us converge to the correct viscosity solution (i.e., the SDF)?* Using properties of viscosity solutions, and PDE theory, we rigorously establish bounds on the INR generalization error. To the best of our knowledge, this is the first such estimate to provide bounds on the error between the learned function and the ground truth SDF in terms of the training error. Our main contributions can be summarized as follows.

- Generalization error bounds are presented to validate that minimizing the PDE residual and surface data fidelity loss can ensure that the estimated solution generalizes well to the viscosity solution.
- We propose a novel regularization term based on the vanishing viscosity method with a dynamically scaled loss.
- We justify this regularization using gradient flow methods for variational formulations and demonstrate its ability to stabilize early training for high-frequency components.
- We compare with current state-of-the-art methods such as DiGS [5] and StEik [52], on several datasets to demonstrate the improvements obtained by using our regularization term.

## 2. Related Work

### 2.1. Surface Reconstruction

Reconstructing surfaces from point clouds is a long-studied problem in computer vision that has proven challenging due to non-uniform point sampling, noisy normal estimations, missing surface regions, and other data imperfections [7]. The problem is highly ill-posed, as there are multiple surfaces that can fit a finite set of points. Traditional methods for solving this problem include triangulation methods [13], Voronoi diagrams [1], and alpha shapes [8]. Implicit function methods using radial basis functions [12] and Poisson surface reconstruction [25] are also well-studied. We refer to [7] for a review of classical reconstruction methods. More recent non-neural network-based approaches include Neural Splines [51], which use kernel formulations arising from infinitely wide shallow networks, and Shape As Points (SAP) [41], which represents surfaces using a

differentiable Poisson solver. Particularly relevant to our work is the recent ViscoGrids method [43], grid-based reconstruction technique incorporating viscosity and coarea priors. This is a non-neural network-based method with a fixed non-decaying viscosity coefficient, unlike us. Methods based on differentiable 3D Gaussian splatting [26] have also been increasingly employed for this task [21, 27, 49].

### 2.2. Implicit Neural Representations

Implicit Neural Representations encoded by neural networks have recently gained significant attention in volumetric representation due to their high resolution and compactness [3, 15, 30, 34, 35, 38, 40, 46–48]. These representations have demonstrated success in encoding shapes through neural networks by learning SDFs [3, 32, 40] or occupancy functions [33]. DeepSDF [40] was the first to propose using neural networks to learn the SDF. However, this method relies on ground truth SDFs for supervision, which is not usually available. SAL [3] proposed learning the SDF directly from point cloud data, constraining the learned function to be zero on the surface. SALD [4] improves upon this by incorporating normal information. IGR [20] introduced the Eikonal loss term to ensure that the learned function is a valid SDF. PHASE [29] proposes a density function that converges to a proper occupancy function, and provides theoretical results based on viscosity solutions. SIREN [48] uses a sine activation function for better representation learning, which allows the computation of higher-order derivatives, as we do in this paper.

DiGS [5] builds on SIREN by adding a constraint on the divergence of the learned function, showing improved performance in the absence of normal information. However, the Laplacian of the SDF corresponds to the mean curvature of the surface and should not be minimized in areas of fine detail. StEik [52] identified an underlying instability in training with the Eikonal loss and proposed minimizing the directional divergence of the network, which is similar in spirit to the gradient-Hessian alignment constraint in [50]. However, when the Eikonal equation is satisfied, this alignment naturally occurs, as far as can be determined from the sample points, and may be a redundant constraint. Moreover, adding a diffusion term can help stabilize spurious geometries during early training. Our training loss integrates a diffusion term directly into the Eikonal loss, providing stabilization without excessive smoothing.

### 2.3. Neural PDE solvers

Partial Differential Equations (PDEs) are foundational models in many applications, including computer graphics and wave propagation. Traditional methods to solve these equations include finite difference methods, finite element methods, etc.; see [2, 28]. In particular, the Fast Marching Method [44] is widely used to solve the Eikonal equation. With recent advances in deep learning, neural networks

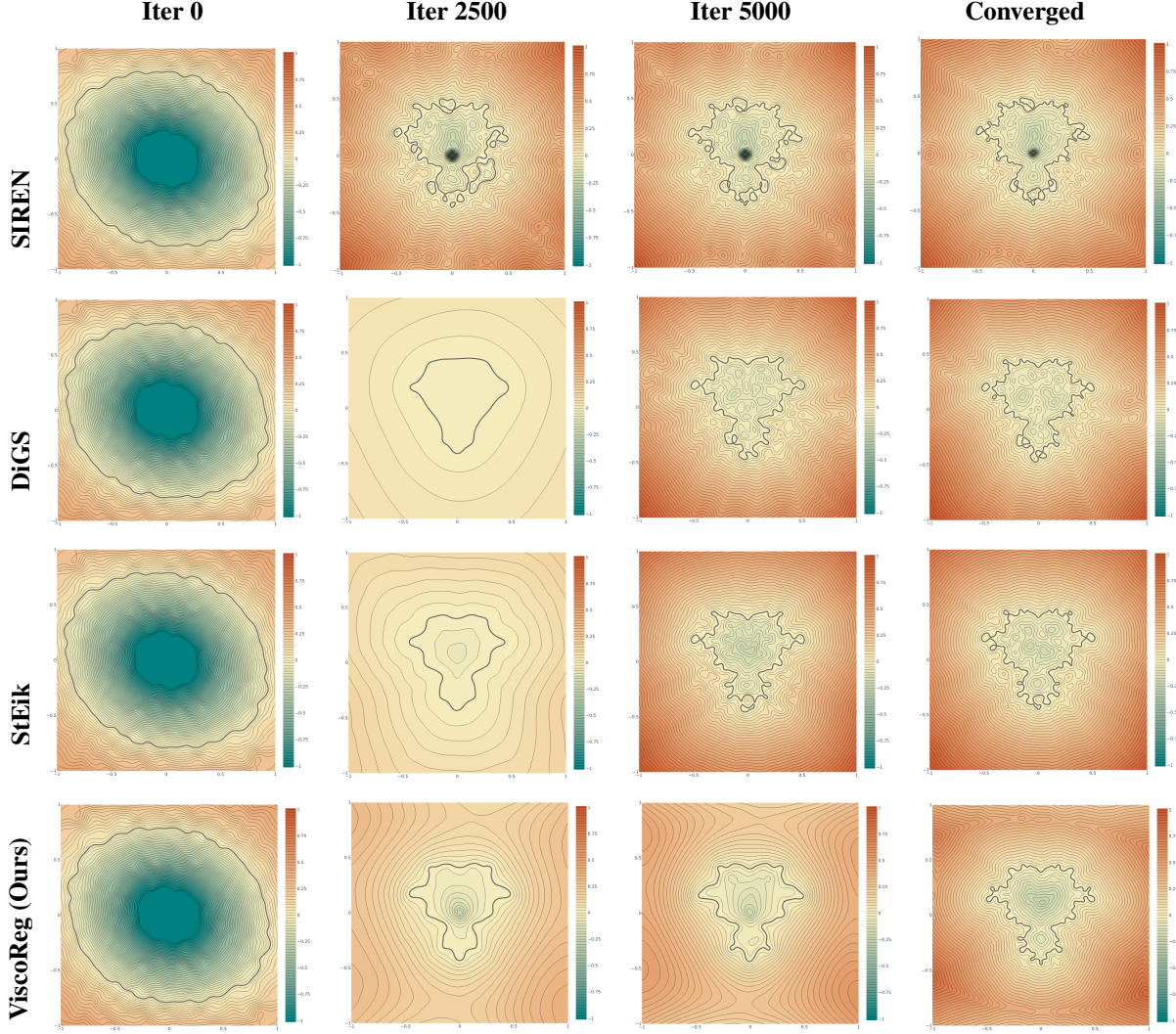


Figure 1. Reconstructing the 2D fractal Mandelbrot set using different Neural SDF techniques. **SIREN**: Converges quickly but the boundary is poorly reconstructed with multiple self-intersections. **DiGS**: Overly smoothed boundary in early iterations, with the final reconstructed boundary being disconnected and self-intersecting. **StEik**: While it avoids oversmoothing, it struggles with spurious self-intersections, disconnections and not capturing fine detail. **ViscoReg**: Smoothly converges to the underlying complex boundary, maintaining its intricate structure throughout training.

have increasingly been used to approximate solutions to PDEs [10, 22, 45]. Among the most notable approaches is the Physics-Informed Neural Network (PINN) framework, introduced by Karniadakis et al. [24], which incorporates PDE residuals and boundary conditions as constraints in the learning process. The Neural SDF method, in fact, can be viewed as a specific form of PINN designed to solve the Eikonal equation. Despite the massive empirical advances, learning theory for neural network-based PDE solvers is still nascent. Generalization theory for networks aims to understand how well the network generalizes to unseen data given the training error. Several results have been established for forward and inverse PINN problems in the ab-

stract setting [36, 37], as well as for various specific classes of PDEs [9, 18, 23, 53]. We aim to extend these results for the Neural SDF to gain intuition on why the network should converge to the correct solution and what the worst-case deviation from the ground truth might be.

### 3. Error Bounds & ViscoReg

First, we give a brief overview on Neural SDF methods and provide the mathematical background relating the Eikonal equation and viscosity solutions, to motivate the ViscoReg regularization.

We use  $\|\cdot\|_p$  to represent the  $L^p$  norm in the corresponding domain for  $1 \leq p \leq \infty$ . The set of continuous functions



on  $\Omega$  is represented by  $C(\Omega)$  and  $C^k(\Omega)$  is the set of  $k$ -th order continuously differentiable functions for  $1 \leq k \leq \infty$ . As usual,  $W^{k,p}(\Omega)$  represents the Sobolev space of functions. We use the classical norms in these spaces, see [19].

### 3.1. Neural Signed Distance Functions

The Neural SDF method trains a neural network  $u_\theta : \Omega \subset \mathbb{R}^3 \rightarrow \mathbb{R}$  parametrized by its weights  $\theta \in \mathbb{R}^d$  to learn an SDF  $u$  implicitly representing a surface manifold  $\partial\Omega$ . Several loss functions are used to supervise this method when a ground truth SDF for non-manifold points are not available. They include the *manifold constraint*  $\mathcal{L}_m$  which enforces that the function is zero for points on the manifold and the *non-manifold penalization constraint*  $\mathcal{L}_{nm}$  to ensure the function is non-zero for non-manifold points. When normals are not available, we also require the *Eikonal constraint*  $\mathcal{L}_{eik}$  that constrains the norm of the gradient to be one. They are defined as:

$$\mathcal{L}_m(u_\theta) = \int_{\partial\Omega} |u_\theta(x)| dx, \quad \mathcal{L}_{nm}(u_\theta) = \int_{\Omega \setminus \partial\Omega} e^{-\alpha|u_\theta(x)|} dx, \quad (3)$$

$$\mathcal{L}_{eik}(u_\theta) = \int_{\Omega} \|\nabla u_\theta\|_2 - 1 \|^p dx \text{ for } p = 1, 2. \quad (4)$$

The combined loss with hyperparameters  $\alpha_m, \alpha_{nm}, \alpha_e$  and  $\alpha \gg 1$  is

$$\mathcal{L}(u_\theta) = \alpha_m \mathcal{L}_m(u_\theta) + \alpha_{nm} \mathcal{L}_{nm}(u_\theta) + \alpha_e \mathcal{L}_{eik}(u_\theta). \quad (5)$$

Ground truth normals must usually be obtained via pre-processing that are prone to errors. Accordingly, normal supervision is not considered here, but can be easily added.

While the loss functions in (3)-(4) are represented with continuous integrals, loss functions are evaluated in practice using mean  $\ell^1$ , and  $\ell^p$  norms evaluated at sample points. We denote the discrete versions of the loss functions  $\mathcal{L}_m, \mathcal{L}_{nm}, \mathcal{L}_{eik}$  as  $L_m, L_{nm}$  and  $L_{eik}$  respectively. The surface point cloud is given as an input, and the computational domain is typically uniformly sampled for non-manifold points, leading to integral approximation errors, discussed later. Given this training regime, we show that the converged solution sufficiently approximates the correct viscosity solution.

### 3.2. Viscosity solutions and Generalization Error

A considerable challenge in the study of the Eikonal equation in (1) is the lack of uniqueness - there exist infinitely many continuous solutions to the equation. For instance, consider the case of the one-dimensional Eikonal equation  $\|u'(x)\|_2 = 1$ , with boundary conditions  $u(0) = u(1) = 0$  in the domain  $[0, 1]$ . Any zig-zag function with slopes  $\pm 1$  satisfying the boundary conditions is a solution (the points with  $C^1$  discontinuities are a set of measure 0). Since the equation is nonlinear, the standard notion of weak solutions

does not apply. However, in many applications, the physically meaningful solution is the *viscosity solution*, introduced by Crandall and Lions [16]. These solutions possess maximum and stability properties, which makes the analysis of Eikonal equation—and more broadly, of the class of Hamilton-Jacobi equations—more tractable. Viscosity solutions inherit these properties from the solutions of the well-posed parabolic equations (2), which they approximate as a limit [11].

Using properties of the viscosity solutions, and classical inequalities in PDE theory, we provide a generalization error estimate for the Neural SDF method. The estimate is provided when  $L^1$  norm is used for the Eikonal loss, however it can easily be extended to the  $p = 2$  case. We follow the approach outlined in [37] for generalization error for solutions to an abstract class of PDEs, and extend it to the Eikonal equation.

The computational domain is often chosen as a bounding box tightly fitted to the surface, enclosing the shape. For purpose of analysis, we simply consider the domain to be the volume enclosed by the surface. Since the trained neural network will not exactly satisfy the Eikonal equation (1), we consider the more general formulation of the boundary value problem (BVP):

$$\|\nabla u(x)\|_2 = f(x), \quad x \in \Omega, \quad u(x) = g(x), \quad x \in \partial\Omega. \quad (6)$$

where  $f \in C^\infty(\bar{\Omega})$ ,  $g \in C(\partial\Omega)$ , for  $\bar{\Omega} = \Omega \cup \partial\Omega$ . When  $f \neq 1$ , the solution  $u \in C(\Omega)$  is not the SDF but rather the shortest arrival time of a wavefront propagating from  $x \in \Omega$  to  $\partial\Omega$ . The function  $f$  represents the "slowness" (reciprocal of the speed) in the medium, while  $g$  acts as an exit-time penalty.

To obtain the required bounds, we establish a few preliminary results using the maximum principle for viscosity solutions, which states that if  $\|\nabla u_1(x)\|_2 \leq \|\nabla u_2(x)\|_2$  for all  $x \in \Omega$ , and  $u_1|_{\partial\Omega} \leq u_2|_{\partial\Omega}$  then  $u_1 \leq u_2$  in  $\bar{\Omega}$ .

**Lemma 1** Suppose  $u_1, u_2 \in C(\Omega)$  are viscosity solutions to (6) with boundary conditions  $u_1|_{\partial\Omega} = g_1, u_2|_{\partial\Omega} = g_2$  with  $g_1, g_2 \in C(\partial\Omega)$ . Let  $\|\nabla u_1\|_2 = \|\nabla u_2\|_2 = 1$ . Then:

$$\|u_1 - u_2\|_\infty \leq \|g_1 - g_2\|_\infty. \quad (7)$$

The proof of this lemma is included in the Supplementary material and follows from results in [11, 17]. Lemma 1 shows that the BVP (6) has at most one continuous viscosity solution since if  $u_1|_{\partial\Omega} = u_2|_{\partial\Omega} = g$ , then  $u_1 = u_2$  in  $\bar{\Omega}$ .

Next, we provide a *stability estimate* that shows the sensitivity of the viscosity solution  $u$  to the slowness function  $f$ . The proof is in the supplementary material [11, 17].

**Lemma 2** Suppose  $u_1$  and  $u_2$  are the unique viscosity solutions to the Eikonal equation with  $u_1, u_2|_{\partial\Omega} = 0$  and



$\|\nabla u_1\|_2 = f_1$  and  $\|\nabla u_2\|_2 = f_2$ . Assume,  $\exists C_f > 0$  such that  $0 < \frac{1}{C_f} \leq f_1, f_2 < C_f$ . Then the solutions satisfy:

$$\|u_1 - u_2\|_\infty \leq C_\Omega C_f^{-2} \|f_1 - f_2\|_\infty. \quad (8)$$

where  $C_\Omega$  is a constant corresponding to the diameter of  $\Omega$ .

We also state the following classical result that follows from the Gagliardo–Nirenberg interpolation inequality relating different norm estimates [39].

**Theorem 1** Let  $\Omega \subset \mathbb{R}^3$  be an open smooth connected domain. For  $u \in L^1(\Omega) \cap W^{6,1}(\Omega)$ , we have:

$$\|u\|_\infty \leq C'_\Omega \|u\|_{W^{6,1}(\Omega)}^{1/2} \|u\|_1^{1/2}. \quad (9)$$

Here  $C'_\Omega$  is a constant depending only on  $\Omega$ .

Note that this result also holds for compact Riemannian manifolds [39].

Let  $\theta^*$  be the local minima to which the optimization problem converged, and let  $u_{\theta^*} \in C^\infty(\Omega)$  be the corresponding neural network. Note that the network output is smooth since we use the sine activation function in SIREN [48]. Then for some  $f_{\theta^*} \in C^\infty(\Omega)$ ,  $g_{\theta^*} \in C^\infty(\partial\Omega)$ , the network satisfies:

$$\|\nabla u_{\theta^*}(x)\|_2 = f_{\theta^*}(x), \quad x \in \Omega, \quad u_{\theta^*}(x) = g_{\theta^*}(x), \quad x \in \partial\Omega. \quad (10)$$

The neural network output  $u_{\theta^*}$  after convergence through the training procedure in 3.1 is assumed to satisfy the following.

**Assumption 1:** There exists  $C_{\theta^*}$  such that the neural network satisfies  $0 < \frac{1}{C_{\theta^*}} \leq \|\nabla u_{\theta^*}\|_2 \leq C_{\theta^*}$ .

If  $\theta^*$  is a sufficiently good local minima, it is natural that Assumption 1 holds, since the ground truth SDF  $u$  satisfies  $\|\nabla u\|_2 = 1 > 0$ .

**Assumption 2:** Let  $S = \{x_i\}_{i=1}^N$  be the input point cloud. We assume there exists  $\beta > 0$  such that the distribution of the point cloud samples satisfies the following quadrature error bound:

$$\left| \int_\Omega |g(x)|^p dx - \frac{1}{N} \sum_{i=1}^N |g(x_i)|^p \right| \leq C_g N^{-\beta}, \quad (11)$$

for  $p = 1, 2$ . This assumption is quite general, essentially requiring that as  $N \rightarrow \infty$ , the sample  $\ell^p$  norm converges to the true  $L^p$  norm. In the case of uniform sampling,  $\beta = 1/3$ , while for Monte-Carlo random sampling [37],  $\beta = 1/2$  for sufficiently smooth functions. However, since the point cloud data may be obtained through sensors, we consider the more general  $\beta$  to account for irregularities in the sampling process. Ignoring measurement errors, we consider the sampling process to be deterministic, while non-uniform.

**Assumption 3:** The residual functions are bounded in the  $W^{6,1}(\Omega)$  Sobolev norm. Specifically,  $\|f_{\theta^*}\|_{W^{6,1}(\Omega)}, \|g_{\theta^*}\|_{W^{6,1}(\partial\Omega)} \leq M_{\theta^*}$  for  $M_{\theta^*} > 0$ . This assumption is automatically satisfied if  $f_{\theta^*}, g_{\theta^*}$  are bounded in  $C^6(\Omega)$  norm since  $\Omega$  is bounded.

**Theorem 2** Let  $|S| = N$  where  $S$  is the set of point-cloud data and let  $M$  be the number of non-manifold points sampled uniformly in the domain. Let  $u_{\theta^*} \in C^\infty(\Omega)$  be the converged neural network obtained through training by the PDE residual and boundary losses (3). Suppose Assumptions 1-3 hold. Denoting  $u \in C(\Omega)$  to be the ground truth SDF, the error is bounded as:

$$\|u - u_{\theta^*}\|_\infty \lesssim M_{\theta^*} (L_m(u_{\theta^*}))^{\frac{1}{2}} + M_{\theta^*} C_{\theta^*}^{-2} (L_{eik}(u_{\theta^*}))^{\frac{1}{2}} + \mathcal{O}((M + N)^{-1/6}) + \mathcal{O}(N^{-\frac{\beta}{2}}). \quad (12)$$

The constants in  $\lesssim$  depend only on  $\bar{\Omega}$ .

*Proof:* From Lemma 1, the Eikonal equation can have at most one continuous viscosity solution. Since  $u_{\theta^*}$  is smooth, it is the unique viscosity solution to the PDE. Define an auxiliary function  $\hat{u}_{\theta^*}$  such that it is the unique viscosity solution of the PDE:

$$\|\nabla \hat{u}_{\theta^*}(x)\|_2 = 1, \quad x \in \Omega, \quad \hat{u}_{\theta^*}(x) = g_{\theta^*}(x), \quad x \in \partial\Omega. \quad (13)$$

From the regularity of  $\partial\Omega$  and  $g_{\theta^*}$ , it follows that  $\hat{u}_{\theta^*} \in C(\Omega)$ . Using the triangle inequality:

$$\|u - u_{\theta^*}\|_\infty \leq \|u - \hat{u}_{\theta^*}\|_\infty + \|\hat{u}_{\theta^*} - u_{\theta^*}\|_\infty. \quad (14)$$

By Lemma 1, we write:

$$\|u - \hat{u}_{\theta^*}\|_\infty \leq \|g_{\theta^*}\|_\infty. \quad (15)$$

From Lemma 2, the second term in (14) can be bounded as:

$$\|\hat{u}_{\theta^*} - u_{\theta^*}\|_\infty \leq C_\Omega C_{\theta^*}^{-2} \|1 - f_{\theta^*}\|_\infty. \quad (16)$$

where  $C_\Omega$  is a constant depending only on the domain. Putting together (15) and (16):

$$\|u - u_{\theta^*}\|_\infty \leq \|g_{\theta^*}\|_\infty + C_\Omega C_{\theta^*}^{-2} \|1 - f_{\theta^*}\|_\infty \quad (17)$$

Using the inequality in Theorem 3 for open bounded sets (here,  $\Omega$ ) and compact Riemannian manifolds (here,  $\partial\Omega$ ), along with Assumption 3:

$$\|u - u_{\theta^*}\|_\infty \lesssim M_{\theta^*} \|g_{\theta^*}\|_1^{\frac{1}{2}} + M_{\theta^*} C_{\theta^*}^{-2} \|1 - f_{\theta^*}\|_1^{\frac{1}{2}}, \quad (18)$$

where the hidden constants in  $\lesssim$  only depends on  $\bar{\Omega}$ . Observe that both  $\|g_{\theta^*}\|_1$  and  $\|1 - f_{\theta^*}\|_1$  can be approximated by their sample norms. The neural SDF method samples

uniformly in the domain for the Eikonal loss  $\|1 - f_{\theta^*}\|_1$  and hence the  $L^1(\Omega)$  quadrature error is  $\mathcal{O}(N^{-1/3})$ , where  $N$  is the number of sample points. Assumption 2 can be used to bound the boundary loss  $\|g_{\theta^*}\|_1$ . This gives:

$$\begin{aligned} \|u - u_{\theta^*}\|_{\infty} &\lesssim M_{\theta^*} \left( \frac{\sum_{i=1}^N g_{\theta^*}(x_i)}{N} \right)^{\frac{1}{2}} + \\ &M_{\theta^*} C_{\theta^*}^{-2} \sqrt{N} \left( \frac{\sum_{i=1}^{M+N} |1 - f_{\theta^*}|_1}{M+N} \right)^{\frac{1}{2}} \\ &+ \mathcal{O}(N^{-\frac{\beta}{2}}) + \mathcal{O}((M+N)^{-1/6}). \end{aligned} \quad (19)$$

Since the first term can be represented using the boundary loss, and the second term by the Eikonal loss, we obtain the required result.  $\square$

At first glance, the generalization bound may seem expected, as it suggests that small training error leads to better generalization. However, this result is non-trivial in the context of PDE solutions, where there is no fundamental reason why minimizing the PDE residual and boundary loss at finitely many points should necessarily lead the network to converge to a solution of the continuous equation. This is particularly insightful in the case of the Eikonal equation, which is ill-posed and admits infinitely many solutions, only one of which is the viscosity solution corresponding to the true SDF. Our result provides a *theoretical guarantee* that the learned function is close to the viscosity solution in the  $L^{\infty}$  sense, offering insight into how training error controls the worst-case deviation from the correct viscosity solution.

### 3.3. Energy Formulations and Gradient Flow

An important problem in many applications is to find a function  $u : \Omega \subset \mathbb{R}^n \rightarrow \mathbb{R}$  that minimizes a functional  $E(u)$ , often representing energy or a loss function. The *gradient flow* of  $E(u)$  is obtained by taking the continuum limit of the gradient descent formulation and is given by:

$$u_t = -\nabla E(u). \quad (20)$$

Here,  $t$  represents the continuous limit of discrete iterations of gradient descent,  $\nabla E(u)$  represents the gradient of  $E$  with respect to  $u$ , defined according to the choice of inner product in the Hilbert space (or the Fréchet derivative of  $E$  with respect to  $u$ ). When  $u$  is restricted to a class of neural networks parametrized by their weights  $\theta$ , denoted as  $u_{\theta}$ , the optimization problem reduces to finding  $\theta$  that minimize  $E(u_{\theta})$ . The gradient descent equation in parameter space becomes:

$$\theta_t = -\nabla_{\theta} E(u_{\theta}). \quad (21)$$

The corresponding equation in function space is a projection of the full gradient descent PDE onto the tangent space

spanned by the neural network’s basis functions [52]. As the network’s representational capacity increases, this basis more closely approximates the full function space, making the projected gradient flow resemble the unconstrained PDE in (20). Therefore we will study the unconstrained gradient flow equation to provide insight into the training process.

The Eikonal loss can be expressed as:

$$L(u) = \int_{\Omega} (\|\nabla u\|_2 - 1)^p dx, \quad p = 1, 2. \quad (22)$$

Computing the Frechet derivative of the loss functional, the gradient flow PDE for the Eikonal loss closely resembles the heat equation with:

$$u_t = \nabla \cdot (g(\|\nabla u\|_2) \nabla u), \quad g(s) = \begin{cases} \frac{1}{s} - 1, & p = 2 \\ \text{sign}(s - 1), & p = 1 \end{cases}$$

Observe that  $g$  can be positive or negative making the above equation a Forward-Backward heat equation. The backward nature tends to destabilize the PDE and is similar to the Perona-Malik equation proposed as a model to remove noise from digital images without blurring edges [42].

The gradient flow of the Eikonal loss has been studied by Yang et al. (2023) [52], who simplified the analysis by assuming  $g(\|\nabla u\|)$  locally a constant. They demonstrate that adding a Laplacian energy term as in [5], or adding a normal supervision term can add stability to the training process. However, since the Laplacian of the SDF corresponds to the mean curvature of the underlying surface, it should not be minimized in areas of fine detail. In other cases, the normals are noisy or not always available. They additionally propose an alternative directional divergence regularizing term, but we demonstrate that our method improves upon StEik’s results while maintaining stability.

### 3.4. ViscoReg

In order to converge to the physically meaningful solution when training a neural SDF function, we propose modifying the Eikonal loss term by adding a decaying viscosity term:

$$\mathcal{L}(u_{\theta}) = \alpha_m \mathcal{L}_m(u_{\theta}) + \alpha_{nm} \mathcal{L}_{nm}(u_{\theta}) + \alpha_v \mathcal{L}_{veik}(u_{\theta}). \quad (23)$$

Here  $\mathcal{L}_{veik}$  represents the viscous Eikonal loss that we refer to as *ViscoReg* given by:

$$\mathcal{L}_{veik}(u_{\theta}) = \int_{\Omega} (\|\nabla u(x)\|_2 - 1 - \varepsilon \Delta u)^p dx, \quad p = 1, 2. \quad (24)$$

Here  $\varepsilon > 0$  is a hyperparameter that we decay to zero in the course of training. For our experiments, we find a linear decay of  $\varepsilon$  to be sufficient. Note that this is different from the DiGS loss because we *do not* want to minimize the divergence with this formulation.

For  $p = 1$ , computing the gradient gives the gradient flow equation to be:

$$\frac{du}{dt} = \nabla \cdot (\text{sign}(1 + \varepsilon \Delta u - \|\nabla u\|_2) \frac{\nabla u}{\|\nabla u\|_2}) - \varepsilon^2 \Delta (\text{sign}(1 + \varepsilon \Delta u - \|\nabla u\|_2) \Delta u) \quad (25)$$

Since the sign function is almost everywhere constant, it can be taken out of the derivative term. Let  $\kappa_e = \text{sign}(1 + \varepsilon \Delta u - \|\nabla u\|_2)$ . Linearising the resulting non-linear PDE around its stationary solution  $u_0 = \mathbf{a} \cdot \mathbf{x}$ , for  $\mathbf{a} = [1, 0, 0]^T$  gives:

$$u_t = \kappa_e \partial_{x_1}^2 u - \kappa_e \varepsilon^2 \Delta u. \quad (26)$$

Taking the Fourier transform of the above PDE gives:

$$\hat{u}_t(t, \omega) = \kappa_e |\omega_1|^2 \hat{u}(t, \omega) - \kappa_e \varepsilon^2 |\omega|^4 \hat{u}(t, \omega) \quad (27)$$

$$\implies \hat{u}(t, \omega) = e^{(\kappa_e |\omega_1|^2 - \kappa_e \varepsilon^2 |\omega|^4)t} \quad (28)$$

Note that for large  $|\omega|$ ,  $\kappa_e > 0$ , and  $\kappa_e |\omega_1|^2 - \kappa_e \varepsilon^2 |\omega|^4 < 0$ . This implies that as  $t \rightarrow \infty$ ,  $\hat{u} \rightarrow 0$  for large frequencies. It also implies that the equation is stable for high frequencies which is exactly the areas of fine detail. Similarly, the gradient flow PDE of this modified loss terms for  $p = 2$  takes the form:

$$\frac{du}{dt} = \nabla \cdot \left( \frac{(\|\nabla u\|_2 - 1)}{\|\nabla u\|_2} \nabla u \right) + \varepsilon \Delta ((\|\nabla u\|_2 - 1) \nabla u) + \varepsilon \nabla (\Delta u \nabla u) - \varepsilon^2 \Delta (\Delta u) \quad (29)$$

Linearizing the second term of the PDE around the stationary linear solution to the above equation  $u = \mathbf{a} \cdot \mathbf{x}$  again gives the linear PDE:

$$\frac{du}{dt} = \partial_{x_1}^2 u + \varepsilon \partial_{x_1} (\Delta u) - \varepsilon^2 \Delta (\Delta u)$$

Taking the Fourier transform of this fourth order PDE:

$$\hat{u}'(t) = -\kappa_e |\omega_1|^2 \hat{u} + i\omega_1^3 \hat{u} - \varepsilon^2 |\omega|^4 \hat{u}. \quad (30)$$

The solution to this ODE is  $\hat{u}(t) = e^{(-|\omega_1|^2 - \varepsilon^2 |\omega|^4 + i\omega_1^3)t}$ . The real part of the exponent is negative for sufficiently large frequencies, again implying stability.

Thus, requiring that in the initial phases of training the solution satisfies the viscous Eikonal PDE over the inviscid version can not only encourage convergence to the physically meaningful solution, but also stabilize the Eikonal training. As proof of concept, we demonstrate the boundary reconstruction of a complicated Mandelbrot fractal with different methods in Figure 1. DiGS, when used without normals, results in an overly smoothed boundary during early iterations. After the annealing phase, where the divergence weight is set to zero, the reconstructed boundary becomes self-intersecting and disconnected. In contrast, VisCoReg smoothly converges to the complex and highly curved boundary, maintaining its intricate structure throughout the process.

## 4. Results

### 4.1. Implementation Details

We evaluate the proposed regularization term on different surface reconstruction tasks. We use the sine activation function proposed in SIREN to compute the second derivatives needed for our task. The method is evaluated on the Surface Reconstruction Benchmark [6], a scene reconstruction task from Sitzmann et al. [48] and Shapenet. All the methods are evaluated on a single Nvidia RTX A6000 GPU. The meshes are extracted using the Marching cubes algorithm [31] using a grid with shortest axis 512 tightly fitted onto the surface. Further implementation details are listed in the supplementary document.

Our main point of comparison involves state-of-the-art methods such as DiGS [5] and StEik [52]. However, note that StEik introduces two key techniques to achieve their results: (1) directional divergence regularizer, (2) quadratic layers in the network architecture. Our work introduces a theoretically motivated regularizer. So, besides the reported results, for an apples-to-apples comparison between the two methods, we include results employing (a) StEik’s regularizer with standard linear layers and the same architecture as our method and (b) StEik’s architecture with our regularizer.

As in [5] and related works, we evaluate our methods on the Chamfer distance metric ( $d_C$ ), and the Hausdorff distance ( $d_H$ ) metric for the Surface Reconstruction Benchmark. For the Shapenet dataset [14], we report the squared Chamfer distance as well as the Intersection over Union (IoU) between the reconstructed shapes and ground truth.

Table 1. Results on SRB dataset. Our method is competitive with SoTA.  $d_C$ : Chamfer distance,  $d_H$ : Hausdorff distance and  $\Delta d_C$ ,  $\Delta d_H$  denote mean deviation from the best performing method.

Method	$d_C$	$d_H$	$\Delta d_C$	$\Delta d_H$
IGR wo n	1.38	16.30	1.2	13.57
SIREN wo n	0.42	7.67	0.23	4.94
SAL	0.36	7.47	0.18	4.74
IGR+FF	0.96	11.06	0.78	8.33
PHASE+FF	0.22	4.96	0.04	2.23
VisCo Grids wo n	0.34	4.39	0.16	1.91
DiGS	0.19	3.52	0.0	0.69
StEik (lin)	0.20	4.56	0.02	1.83
Ours (lin)	<b>0.18</b>	2.96	0.0	0.19
StEik (quad)	<b>0.18</b>	2.80	0.0	0.07
Ours (quad)	<b>0.18</b>	<b>2.73</b>	0.0	0.0

### 4.2. Surface Reconstruction Benchmark (SRB)

SRB consists of five noisy shapes, and contain point clouds and normals. For a fair evaluation, we compare our normal-free method with the normal-free versions of SoTA. To train the network, we used 5 hidden layers, and 128 neurons. For the  $\varepsilon$  parameter, we used an annealing strategy where we set it to  $\varepsilon = 1$  initially and decayed it continuously through



Table 2. Ablation on  $\varepsilon$  decay for dC in SRB. BL  $\times x$ = baseline scaled by  $x$ .

Method	$d_C \downarrow$	$d_H \downarrow$
BL	<b>0.15</b>	<b>1.44</b>
BL $\times 2$	0.16	1.54
BL $\times 0.5$	0.16	1.34
Piecewise Const.	0.16	1.82
Quintic	0.17	2.11
Fast decay (0 @ 20%)	0.16	2.34
Slow decay(0 @ 90%)	0.16	1.68
$\varepsilon = 0$ (SIREN [47])	0.34	6.27
SoTA best (DiGS)	0.15	1.70

piece-wise linear decay to zero. Note that this decay method does not add extra hyperparameters because a similar annealing strategy was used for the divergence term in DiGS. We used the MFGI initialization proposed in [5] to initialize the network. Results were reported on the Chamfer and Hausdorff distances between ground truth meshes in Table 1. Our method improves upon all other methods in this task. There is considerable improvement in the Hausdorff distance but the improvements in Chamfer distance are minor. However, it is noteworthy that we use approximately 25% fewer parameters than DiGs or SIREN for this task.

#### 4.2.1. Viscosity parameter decay ablation

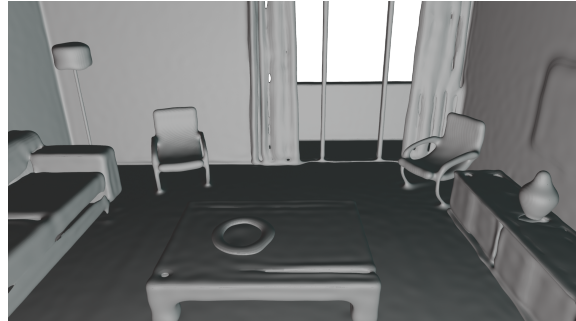
We used a piecewise linear  $\varepsilon$ -decay. For SRB, we used the same decay rate for all but one shape. See Tab. 2 for ablation. Baseline decay is initial  $\varepsilon = 1$ , decayed linearly at 20/40/60/80% iterations to 0.8/0.08/0.01/0. Many “reasonable” decays work well; a schedule surpassing SoTA may be obtained via coarse grid search.

### 4.3. Scene Reconstruction

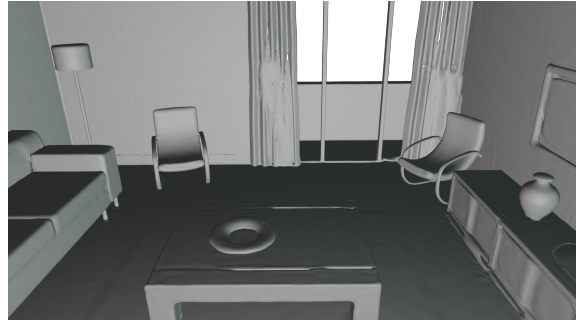
We evaluate on the scene reconstruction task from Sitzmann et al [47]. We use 8 layers and 512 neurons with 10M sample points as in the original dataset. Qualitative results are presented in Figure 2. In the absence of normal information, methods like SIREN report ghost geometries [5]. Due to the smoothing effect of the Laplacian term, the DiGS method does not recover fine details such as sofa legs, vase and picture frames. StEik recovers details somewhat better but still struggles with more intricate detailing like picture frames, curtains, and the plate rim. ViscoReg gives a good result even though we do not use normal information. Our method recovers the fine details reconstructing the surface with greater fidelity.

#### 4.4. Shapenet

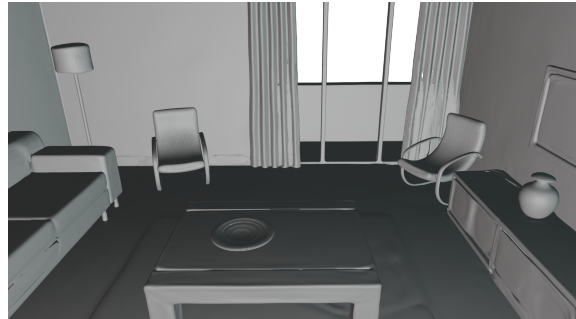
The ShapeNet dataset [14] consists of 3D CAD models spanning a variety of object categories. Following the pre-processing and dataset split of Williams et al. [51], we eval-



(a) DiGS



(b) StEik



(c) ViscoReg (ours)

Figure 2. Results from the scene reconstruction benchmark from [47]. The DiGS mesh (a) is missing fine details like the sofa legs, accurate vase shape on the right, and picture frame details. StEik (b) performs better but struggles with fine details such as the curtains and plate on the table. The ViscoReg mesh (c) reconstructs fine details with high fidelity.

uate on 20 shapes per category across 13 categories. Their preprocessing pipeline ensures consistent normal orientations and converts internal structures into manifold meshes. We use an architecture of 4 hidden layers, and 256 channels for this experiment, as in [5]. We use the MFGI initialization proposed in DiGS for this experiment.

The results in Table 3 and Figure 3 clearly demonstrate quantitative and qualitative improvements with respect to the state of the art method. Our proposed regularization shows significant decrease in the mean squared Chamfer distance, while also showing improvement in IoU. This demonstrates that the proposed regularization can help con-

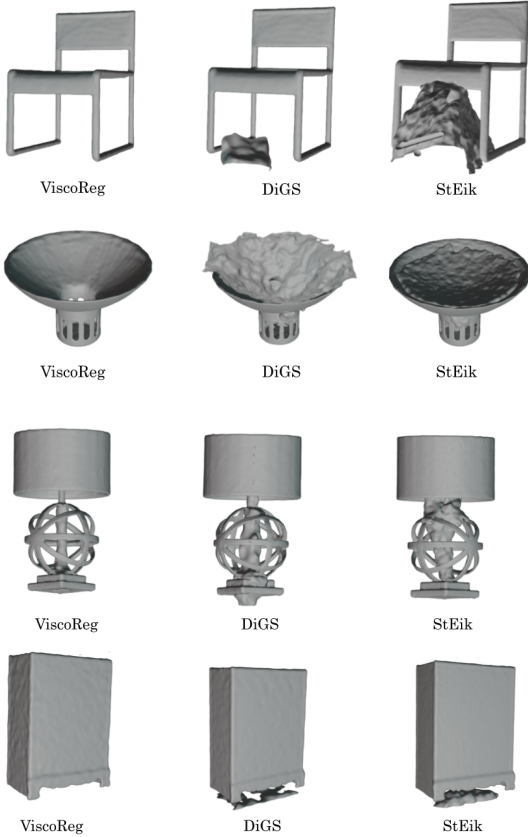


Figure 3. Results from Shapenet [14] for examples drawn from the Chair (top), Lamp (middle two), and Cabinet (right) categories. The DiGS and StEik results show many pieces that should be distinct coalescing into each other, lack of sharp details being maintained, ghost pieces, and other artifacts. The ViscoReg mesh is able to overcome the ghost geometry and reconstruct fine surface details with high fidelity.

verge to better local minima that stabilizes without smoothing out fine details and thin structures.

## 5. Conclusion

In this paper, we aim to provide theoretical insight and improve stability when training neural networks to learn a signed distance function. We leverage classical PDE theory to provide an estimate on the worst case error when using neural networks to approximate the SDF. We also propose a physically-motivated regularizing term (ViscoReg) for improved reconstruction. We demonstrate the effectiveness of our approach on many benchmarks and show increased performance compared to SoTA.

A fundamental challenge, shared by most theoretical guarantees in neural networks, is their difficulty in practical validation. However, such theoretical understanding is critical for providing insight into neural representations and

Table 3. Our method is top 2 in every metric compared to SoTA, showing significant improvement in mean squared Chamfer distances.

method	Squared Chamfer ↓			IoU ↑		
	mean	median	std	mean	median	std
SPSR	2.22e-4	1.7e-4	1.76e-4	0.643	0.673	0.158
IGR	5.13e-4	1.13e-4	2.15e-3	0.810	0.848	0.152
SIREN	1.03e-4	5.28e-5	1.93e-4	0.827	0.910	0.233
FFN	9.12e-5	8.65e-5	3.36e-5	0.822	0.840	0.098
NSP	5.36e-5	4.06e-5	3.64e-5	0.897	0.923	0.087
DiGS +n	2.74e-4	2.32e-5	9.90e-4	0.920	0.977	0.199
SIREN wo n	3.08e-4	2.58e-4	3.26e-4	0.309	0.295	0.201
SAL	1.14e-3	2.11e-4	3.63e-3	0.403	0.394	0.272
DiGS	1.32e-4	2.55e-5	4.73e-4	0.939	0.974	0.126
StEik (lin)	1.36e-4	2.34e-5	9.34e-4	<b>0.963</b>	<b>0.981</b>	0.091
ViscoReg (lin)	<b>5.27e-5</b>	<b>2.32e-5</b>	<b>1.08e-4</b>	0.952	0.978	<b>0.083</b>
StEik (quad)	6.86e-5	<b>6.33e-6</b>	3.34e-4	<b>0.967</b>	<b>0.984</b>	0.088
ViscoReg(quad)	<b>3.98e-5</b>	2.19e-5	<b>7.38e-5</b>	0.959	<b>0.984</b>	0.086

guiding future advancements.

One limitation of our regularization method is the fine-tuning of the viscosity coefficient decay,  $\varepsilon$ . A more principled approach—adjusting  $\varepsilon$  adaptively, increasing it in regions with higher error—could further enhance performance.

## Acknowledgements

MK and RD were supported by ONR Award N00014-23-1-2086 and a Dolby gift.

## References

- [1] Nina Amenta, Marshall Bern, and Manolis Kamvyselis. A new Voronoi-based surface reconstruction algorithm. In *Proceedings of the 25th annual conference on Computer graphics and interactive techniques*, pages 415–421, 1998. 2
- [2] William F Ames. *Numerical methods for partial differential equations*. Academic press, 2014. 2
- [3] Matan Atzmon and Yaron Lipman. SAL: Sign agnostic learning of shapes from raw data. In *Proceedings of the IEEE/CVF conference on computer vision and pattern recognition*, pages 2565–2574, 2020. 2
- [4] Matan Atzmon and Yaron Lipman. SALD: Sign agnostic learning with derivatives. *arXiv preprint arXiv:2006.05400*, 2020. 1, 2
- [5] Yizhak Ben-Shabat, Chamin Hwa Koneputugodage, and Stephen Gould. DiGS: Divergence guided shape implicit neural representation for unoriented point clouds. In *Proceedings of the IEEE/CVF Conference on Computer Vision and Pattern Recognition*, pages 19323–19332, 2022. 1, 2, 6, 7, 8, 12
- [6] Matthew Berger, Joshua A Levine, Luis Gustavo Nonato, Gabriel Taubin, and Claudio T Silva. A benchmark for surface reconstruction. *ACM Transactions on Graphics (TOG)*, 32(2):1–17, 2013. 7
- [7] Matthew Berger, Andrea Tagliasacchi, Lee M Seversky, Pierre Alliez, Gael Guennebaud, Joshua A Levine, Andrei

- Sharf, and Claudio T Silva. A survey of surface reconstruction from point clouds. In *Computer Graphics Forum*, pages 301–329. Wiley Online Library, 2017. 2
- [8] Fausto Bernardini, Joshua Mittleman, Holly Rushmeier, Cláudio Silva, and Gabriel Taubin. The ball-pivoting algorithm for surface reconstruction. *IEEE transactions on visualization and computer graphics*, 5(4):349–359, 2002. 2
- [9] Julius Berner, Philipp Grohs, and Arnulf Jentzen. Analysis of the generalization error: Empirical risk minimization over deep artificial neural networks overcomes the curse of dimensionality in the numerical approximation of black-scholes partial differential equations. *SIAM Journal on Mathematics of Data Science*, 2(3):631–657, 2020. 3
- [10] Jan Blechschmidt and Oliver G Ernst. Three ways to solve partial differential equations with neural networks—a review. *GAMM-Mitteilungen*, 44(2):e202100006, 2021. 3
- [11] Jeff Calder. Lecture notes on viscosity solutions. *Lecture notes*, 2018. 4, 12
- [12] Jonathan C Carr, Richard K Beatson, Jon B Cherrie, Tim J Mitchell, W Richard Fright, Bruce C McCallum, and Tim R Evans. Reconstruction and representation of 3D objects with radial basis functions. In *Proceedings of the 28th annual conference on Computer graphics and interactive techniques*, pages 67–76, 2001. 2
- [13] Frédéric Cazals and Joachim Giesen. Delaunay triangulation based surface reconstruction. In *Effective computational geometry for curves and surfaces*, pages 231–276. Springer, 2006. 2
- [14] Angel X Chang, Thomas Funkhouser, Leonidas Guibas, Pat Hanrahan, Qixing Huang, Zimo Li, Silvio Savarese, Manolis Savva, Shuran Song, Hao Su, et al. Shapenet: An information-rich 3d model repository. *arXiv preprint arXiv:1512.03012*, 2015. 7, 8, 9, 14
- [15] Zhiqin Chen and Hao Zhang. Learning implicit fields for generative shape modeling. In *Proceedings of the IEEE/CVF conference on Computer Vision and Pattern Recognition*, pages 5939–5948, 2019. 2
- [16] Michael G Crandall and Pierre-Louis Lions. Viscosity solutions of Hamilton-Jacobi equations. *Transactions of the American mathematical society*, 277(1):1–42, 1983. 1, 4
- [17] Michael G Crandall, Lawrence C Evans, and P-L Lions. Some properties of viscosity solutions of Hamilton-Jacobi equations. *Transactions of the American Mathematical Society*, 282(2):487–502, 1984. 4
- [18] Tim De Ryck and Siddhartha Mishra. Error analysis for physics-informed neural networks (PINNs) approximating Kolmogorov PDEs. *Advances in Computational Mathematics*, 48(6):79, 2022. 3
- [19] Lawrence C Evans. *Partial differential equations*. American Mathematical Society, 2022. 4
- [20] Amos Gropp, Lior Yariv, Niv Haim, Matan Atzmon, and Yaron Lipman. Implicit geometric regularization for learning shapes. *arXiv preprint arXiv:2002.10099*, 2020. 1, 2
- [21] Antoine Guédon and Vincent Lepetit. Sugar: Surface-aligned gaussian splatting for efficient 3d mesh reconstruction and high-quality mesh rendering. In *Proceedings of the IEEE/CVF Conference on Computer Vision and Pattern Recognition*, pages 5354–5363, 2024. 2
- [22] Jiequn Han, Arnulf Jentzen, and Weinan E. Solving high-dimensional partial differential equations using deep learning. *Proceedings of the National Academy of Sciences*, 115(34):8505–8510, 2018. 3
- [23] Zheyuan Hu, Ameya D Jagtap, George Em Karniadakis, and Kenji Kawaguchi. When do extended physics-informed neural networks (XPINNs) improve generalization? *arXiv preprint arXiv:2109.09444*, 2021. 3
- [24] George Em Karniadakis, Ioannis G Kevrekidis, Lu Lu, Paris Perdikaris, Sifan Wang, and Liu Yang. Physics-informed machine learning. *Nature Reviews Physics*, 3(6):422–440, 2021. 3
- [25] Michael Kazhdan, Matthew Bolitho, and Hugues Hoppe. Poisson surface reconstruction. In *Proceedings of the fourth Eurographics symposium on Geometry processing*, 2006. 2
- [26] Bernhard Kerbl, Georgios Kopanas, Thomas Leimkühler, and George Drettakis. 3d gaussian splatting for real-time radiance field rendering. *ACM Trans. Graph.*, 42(4):139–1, 2023. 2
- [27] Meenakshi Krishnan, Liam Fowl, and Ramani Duraiswami. 3d gaussian splatting with normal information for mesh extraction and improved rendering. *arXiv preprint arXiv:2501.08370*, 2025. 2
- [28] Randall J LeVeque. *Numerical methods for conservation laws*. Springer, 1992. 2
- [29] Yaron Lipman. Phase transitions, distance functions, and implicit neural representations. *arXiv preprint arXiv:2106.07689*, 2021. 2
- [30] Stephen Lombardi, Tomas Simon, Jason Saragih, Gabriel Schwartz, Andreas Lehrmann, and Yaser Sheikh. Neural volumes: Learning dynamic renderable volumes from images. *arXiv preprint arXiv:1906.07751*, 2019. 2
- [31] William E Lorensen and Harvey E Cline. Marching cubes: A high resolution 3d surface construction algorithm. In *Seminal graphics: pioneering efforts that shaped the field*, pages 347–353. 1998. 7, 12
- [32] Baorui Ma, Zhizhong Han, Yu-Shen Liu, and Matthias Zwicker. Neural-pull: Learning signed distance functions from point clouds by learning to pull space onto surfaces. *arXiv preprint arXiv:2011.13495*, 2020. 2
- [33] Lars Mescheder, Michael Oechsle, Michael Niemeyer, Sebastian Nowozin, and Andreas Geiger. Occupancy networks: Learning 3D reconstruction in function space. In *Proceedings of the IEEE/CVF conference on Computer Vision and Pattern Recognition*, pages 4460–4470, 2019. 1, 2, 12
- [34] Mateusz Michalkiewicz, Jhony K Pontes, Dominic Jack, Mahsa Baktashmotlagh, and Anders Eriksson. Implicit surface representations as layers in neural networks. In *Proceedings of the IEEE/CVF International Conference on Computer Vision*, pages 4743–4752, 2019. 2
- [35] Ben Mildenhall, Pratul P Srinivasan, Matthew Tancik, Jonathan T Barron, Ravi Ramamoorthi, and Ren Ng. NeRF: Representing scenes as neural radiance fields for view synthesis. *Communications of the ACM*, 65(1):99–106, 2021. 1, 2
- [36] Siddhartha Mishra and Roberto Molinaro. Estimates on the generalization error of physics-informed neural networks for



- approximating a class of inverse problems for PDEs. *IMA Journal of Numerical Analysis*, 42(2):981–1022, 2022. 3
- [37] Siddhartha Mishra and Roberto Molinaro. Estimates on the generalization error of physics-informed neural networks for approximating PDEs. *IMA Journal of Numerical Analysis*, 43(1):1–43, 2023. 3, 4, 5
- [38] Thomas Müller, Alex Evans, Christoph Schied, and Alexander Keller. Instant neural graphics primitives with a multiresolution hash encoding. *ACM transactions on graphics (TOG)*, 41(4):1–15, 2022. 2
- [39] Louis Nirenberg. On elliptic partial differential equations. *Annali della Scuola Normale Superiore di Pisa-Scienze Fisiche e Matematiche*, 13(2):115–162, 1959. 5, 12
- [40] Jeong Joon Park, Peter Florence, Julian Straub, Richard Newcombe, and Steven Lovegrove. DeepSDF: Learning continuous signed distance functions for shape representation. In *Proceedings of the IEEE/CVF conference on computer vision and pattern recognition*, pages 165–174, 2019. 1, 2
- [41] Songyou Peng, Chiyu Jiang, Yiyi Liao, Michael Niemeyer, Marc Pollefeys, and Andreas Geiger. Shape as points: A differentiable Poisson solver. *Advances in Neural Information Processing Systems*, 34:13032–13044, 2021. 2
- [42] Pietro Perona and Jitendra Malik. Scale-space and edge detection using anisotropic diffusion. *IEEE Transactions on pattern analysis and machine intelligence*, 12(7):629–639, 1990. 6
- [43] Albert Pumarola, Artsiom Sanakoyeu, Lior Yariv, Ali Thabet, and Yaron Lipman. VisCo grids: Surface reconstruction with viscosity and coarea grids. *Advances in Neural Information Processing Systems*, 35:18060–18071, 2022. 2
- [44] James A Sethian. Fast marching methods. *SIAM review*, 41(2):199–235, 1999. 2
- [45] Justin Sirignano and Konstantinos Spiliopoulos. DGM: A deep learning algorithm for solving partial differential equations. *Journal of computational physics*, 375:1339–1364, 2018. 3
- [46] Vincent Sitzmann, Justus Thies, Felix Heide, Matthias Nießner, Gordon Wetzstein, and Michael Zollhofer. Deepvoxels: Learning persistent 3D feature embeddings. In *Proceedings of the IEEE/CVF Conference on Computer Vision and Pattern Recognition*, pages 2437–2446, 2019. 2
- [47] Vincent Sitzmann, Michael Zollhöfer, and Gordon Wetzstein. Scene representation networks: Continuous 3D-structure-aware neural scene representations. *Advances in Neural Information Processing Systems*, 32, 2019. 8, 13, 14
- [48] Vincent Sitzmann, Julien Martel, Alexander Bergman, David Lindell, and Gordon Wetzstein. Implicit neural representations with periodic activation functions. *Advances in Neural Information Processing Systems*, 33:7462–7473, 2020. 2, 5, 7
- [49] Joanna Waczyńska, Piotr Borycki, Sławomir Tadeja, Jacek Tabor, and Przemysław Spurek. Games: Mesh-based adapting and modification of gaussian splatting. *arXiv preprint arXiv:2402.01459*, 2024. 2
- [50] Ruian Wang, Zixiong Wang, Yunxiao Zhang, Shuangmin Chen, Shiqing Xin, Changhe Tu, and Wenping Wang. Aligning gradient and hessian for neural signed distance function. *Advances in Neural Information Processing Systems*, 36:63515–63528, 2023. 2
- [51] Francis Williams, Matthew Trager, Joan Bruna, and Denis Zorin. Neural splines: Fitting 3D surfaces with infinitely-wide neural networks. In *Proceedings of the IEEE/CVF Conference on Computer Vision and Pattern Recognition*, pages 9949–9958, 2021. 2, 8, 12
- [52] Huizong Yang, Yuxin Sun, Ganesh Sundaramoorthi, and Anthony Yezzi. StEik: Stabilizing the optimization of neural signed distance functions and finer shape representation. *Adv. Neural Inform. Process. Syst.*, 36:13993–14004, 2023. 1, 2, 6, 7, 12
- [53] Kirill Zubov, Zoe McCarthy, Yingbo Ma, Francesco Calisto, Valerio Pagliarino, Simone Azeglio, Luca Bottero, Emmanuel Luján, Valentin Sulzer, Ashutosh Bharambe, et al. Neuralpde: Automating physics-informed neural networks (pinns) with error approximations. *arXiv preprint arXiv:2107.09443*, 2021. 3

## 6. Supplementary Material

In this section, we provide supplementary details for our paper.

### 6.1. Mathematical Proofs

#### 6.1.1. Proof of Lemma 1

Let  $C = \max_{\partial\Omega} \|u - v\|$ . Then by definition:

$$u(x) - C \leq v(x), \quad x \in \partial\Omega. \quad (31)$$

The function  $u(x) - C$  is a solution to another Eikonal equation as well with  $\|\nabla(u - C)\| = 1$ . A classical result (see Corollary 3.2 in [11]) then implies that:

$$u(x) - C \leq v(x) \quad x \in \Omega \quad (32)$$

$$\implies u(x) - v(x) \leq \max_{\partial\Omega} (u - v), \quad \forall x \in \Omega \quad (33)$$

This bound may also be obtained for  $v - u$  by flipping  $u$  and  $v$ . It follows that,

$$\|u - v\|_\infty \leq \max_{\partial\Omega} \|u - v\| = \|g_1 - g_2\|_\infty \quad (34)$$

#### 6.1.2. Proof of Lemma 2

Let  $\hat{f}_1 = \lambda f_1$  where  $\lambda = \max_{\Omega} \frac{f_2}{f_1}$ . By construction, this ensures that  $\hat{f}_1 \geq f_2$ . Note that  $\lambda u_1$  is the viscosity solution to the Eikonal equation with slowness  $\hat{f}_1$ . Since  $\lambda u_1, u_2$  are the viscosity solutions, they obey the maximum principle, and hence  $\lambda u_1 \geq u_2$ . This leads to the following inequality:

$$\begin{aligned} u_2 - u_1 &\leq (\lambda - 1)u_1 \leq \max_{\Omega} \frac{f_2 - f_1}{f_1} u_1 \\ &\leq \frac{1}{C_f} \|f_1 - f_2\|_\infty u_1. \end{aligned} \quad (35)$$

Since  $u_1$  is the signed distance function, it can be bounded by the maximum time to travel between two points in the domain, and hence,

$$\|u_1\|_\infty \leq C(\Omega) C_f^{-1}. \quad (36)$$

Inequality (35) may also be derived for  $u_1 - u_2$  by swapping  $u_1$  and  $u_2$ . Consequently:

$$\|u_1 - u_2\|_{L^\infty(\Omega)} \leq C_\Omega C_f^{-2} \|f_1 - f_2\|_\infty \quad (37)$$

#### 6.1.3. Generalization error for $L^2$ Eikonal Loss

The  $L^2$  error estimate may be obtained in a similar setting as Theorem 2 by using a more general version of Theorem 1 that we state below.

**Theorem 3 [39]** *Let  $\Omega \subset \mathbb{R}^3$  be an open smooth connected domain. Let  $1 \leq r, m \leq \infty$  and  $\alpha \in [0, 1]$  such that:*

$$(1 - \alpha) \left( \frac{m}{3} - \frac{1}{r} \right) = \frac{\alpha}{p} \quad (38)$$

for  $p = 1, 2$ . Then for  $u \in L^1(\Omega) \cap W^{m,r}(\Omega)$ , we have:

$$\|u\|_\infty \leq \|u\|_{W^{m,r}(\Omega)}^{1-\alpha} \|u\|_p^\alpha. \quad (39)$$

By following the proof of Theorem 2, with this inequality, we can provide a similar result.

### 6.2. Implementation Details

For testing for all shapes, we use the Marching Cubes algorithm [31] with resolution 512 and the same mesh extraction process as [52], [5] and other methods.

#### 6.2.1. Surface Reconstruction Benchmark

First, we center the input point clouds at the origin and normalize them so that it is inside the unit cube. The bounding box is scaled to 1.1 times the size of the shape. At each iteration, we sample 15,000 points from the original point cloud and an additional 15,000 points uniformly from the bounding box. Training is conducted for 10,000 iterations with a learning rate of  $10^{-4}$ . The weights were taken to be  $[\alpha_m, \alpha_{nm}, \alpha_e] = [3000, 100, 50]$ . Baseline decay for all shapes but one is initial  $\varepsilon = 1$ , decayed linearly at 20/40/60/80% iterations to 0.8/0.08/0.01/0. The shape `lordquas` benefited from a different linear decay setting at 20/40/60/80% iterations to 0.5/0.2/0.05/0. We used 5 hidden layers, and 128 nodes. MFGI with sphere initial parameters was taken to be (1.6, 0.1).

For the results with quadratic neurons, we used the same architecture as StEik [52] and the decay rate is taken to be decaying linearly at 40%/60% iterations to 0.01/0.0 for all but `anchor` and `gargoyle`. For these shapes we take linear decay at 60%, 80% iterations to 0.03/0.0.

Additional quantitative results for each individual shape are presented in Table 4.

#### 6.2.2. Scene Reconstruction

For this experiment, we used an architecture of 8 hidden layers, and 512 channels. At each iteration, we sample 15,000 points from the original point cloud and another 15,000 points uniformly at random within the bounding box. Training is performed for 100,000 iterations with a learning rate of  $8 \times 10^{-6}$ . The weights used were  $[\alpha_m, \alpha_{nm}, \alpha_e] = [5000, 100, 50]$ . The viscosity coefficient  $\varepsilon$  decayed piecewise linearly starting at 0.5, decaying to 0.01 at 50 percent iterations followed by steeply decaying to 0 at 60 percent.

#### 6.2.3. Shapenet

We follow the preprocessing and evaluation methodology outlined in [51]. First, the preprocessing technique from [33] is applied, then performance is evaluated on the first 20 shapes of the test set for each shape class. The preprocessing step extracts ground truth surface points from

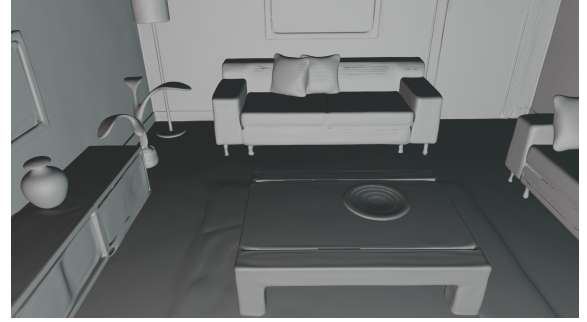
Shape	Method	$d_C$	$d_H$
Overall	IGR wo n	1.38	16.33
	SIREN wo n	0.42	7.67
	SAL	0.36	7.47
	IGR+FF	0.96	11.06
	PHASE+FF	0.22	4.96
	DiGS	0.19	3.52
	StEik	<b>0.18</b>	2.80
	ViscoReg	<b>0.18</b>	2.96
	ViscoReg (quad)	<b>0.18</b>	<b>2.73</b>
Anchor	IGR wo n	0.45	7.45
	SIREN wo n	0.72	10.98
	SAL	0.42	7.21
	IGR+FF	0.72	9.48
	PHASE+FF	0.29	7.43
	DiGS	0.29	7.19
	StEik	0.26	4.26
	ViscoReg	<b>0.25</b>	5.36
	ViscoReg (quad)	<b>0.24</b>	<b>4.18</b>
Daratech	IGR wo n	4.9	42.15
	SIREN wo n	0.21	4.37
	SAL	0.62	13.21
	IGR+FF	2.48	19.6
	PHASE+FF	0.35	7.24
	DiGS	0.20	3.72
	StEik	0.18	<b>1.72</b>
	ViscoReg	0.18	2.94
	ViscoReg (quad)	<b>0.17</b>	1.98
DC	IGR wo n	0.63	10.35
	SIREN wo n	0.34	6.27
	SAL	0.18	3.06
	IGR+FF	0.86	10.32
	PHASE+FF	0.19	4.65
	DiGS	<b>0.15</b>	1.70
	StEik	0.16	1.73
	ViscoReg	<b>0.15</b>	1.44
	ViscoReg (quad)	0.16	<b>1.35</b>
Gargoyle	IGR wo n	0.77	17.46
	SIREN wo n	0.46	7.76
	SAL	0.45	9.74
	IGR+FF	0.26	5.24
	PHASE+FF	<b>0.17</b>	4.79
	DiGS	<b>0.17</b>	4.10
	StEik	0.18	4.49
	ViscoReg	<b>0.17</b>	<b>3.96</b>
	ViscoReg (quad)	0.18	4.50
Lord Quas	IGR wo n	0.16	4.22
	SIREN wo n	0.35	8.96
	SAL	0.13	4.14
	IGR+FF	0.49	10.71
	PHASE+FF	<b>0.11</b>	<b>0.71</b>
	DiGS	0.12	0.91
	StEik	0.13	1.81
	ViscoReg	0.14	1.09
	ViscoReg (quad)	0.13	1.69



(a) DiGS



(b) StEik



(c) ViscoReg (ours)

Figure 4. Results from the scene reconstruction benchmark from [47]. The DiGS mesh (a) is missing fine details like the sofa legs, accurate vase shape on the right, and picture frame details. StEik (b) performs better but struggles with fine details such as the curtains and plate on the table. The overall quality of mesh requires improvement. The ViscoReg mesh (c) reconstructs fine details with high fidelity.

ShapeNet and generates random samples within the domain, and their corresponding occupancy values. For evaluation, the ground truth surface points are used to compute the squared Chamfer distance, while the labeled random samples are used to calculate the Intersection over Union (IoU).

During training, 15,000 points are sampled from the original point cloud and an additional 15,000 points are sampled uniformly at random within the bounding box. The model is trained for 10,000 iterations with a learning rate of  $5 \times 10^{-5}$ . The weights were chosen to be  $[\alpha_m, \alpha_{nm}, \alpha_e] =$

Table 4. Additional quantitative results on the Surface Reconstruction Benchmark using point data without normals.



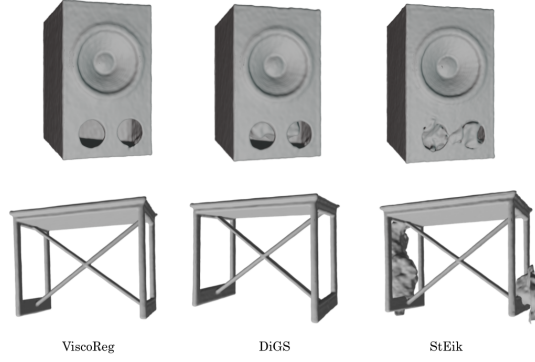


Figure 5. Quantitative results from ShapeNet dataset [14].

[5000, 100, 50]. The viscosity coefficient  $\varepsilon$  decayed piecewise linearly starting at 1.0 decreasing at 10%, 20%, 30% and 40% to 0.0 for all shapes besides rifle, lamp, and table. For these shapes, we start the decay at  $\varepsilon = 10.0$ .

Additional quantitative results are provided in Figure 5.

#### 6.2.4. Faster Convergence

We demonstrate ViscoReg’s faster convergence to better minima (in terms of the Eikonal constraint) than SIREN [47] with unstable Eikonal loss (see Fig 6).

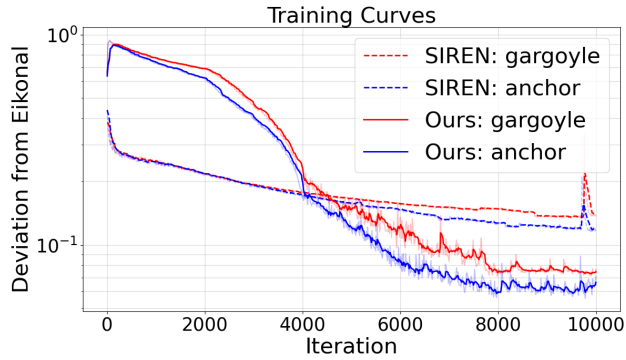


Figure 6. Deviation from Eikonal.